Linear and Nonlinear Elastic Waves in Magnetogranular Chains

F. Allein,[*] V. Tournat, V. Gusev, and G. Theocharis[†]
LAUM, UMR-CNRS 6613, Le Mans Université, Avenue O. Messiaen, 72085 Le Mans, France

We study a magnetogranular chain composed of stainless-steel beads which are placed inside an appropriately designed periodic magnetic field. The latter provides attractive forces between the particles, leading to a stable structure, free of mechanical boundaries. Using a scanning laser-based probe at the individual-particle level, we observe experimentally the propagation of longitudinal as well as transverse-rotational waves. In addition, we obtain the dispersion band diagram. In the linear regime, these observations are well supported by a mass-spring model that takes into account both a normal and a shear mechanical coupling between the beads, considering translational and rotational degrees of freedom. In the weakly nonlinear regime, we present experimental results including beating in the amplitude of the second harmonic for the longitudinal waves and propagation under oblique driving excitation. A theoretical model that takes into account the Hertzian contact mechanics, dissipation, and the finite size of the system captures well the results for second-harmonic generation with longitudinal waves. This magnetosensitive system offers great freedom to design complex waveguide geometries where the interplay between geometry, wave polarization, and nonlinearity may pave the way toward the development of advanced signal-processing elastic devices.

I. INTRODUCTION

Granular crystals, periodic arrangements of tightly packed elastic beads, have become a particularly appealing platform for the theoretical and experimental study of a plethora of wave phenomena in mechanical structures. The highly nonlinear response of granular crystals, originating from the normal Hertzian contact law [1] between adjacent particles, has been the driving force for numerous theoretical and experimental studies in recent years, including the direct observation of solitary waves [2,3], nonlinear waves [4–6], breathers [7,8], and other effects (see for example Ref. [9] and references therein). In addition, several different engineering applications based on granular chains, including tunable switches, rectifiers, and vibration filters [10–12], have already been proposed.

However, there is another feature of granular crystals on which there has been a certain silence over these years: the rotational degrees of freedom. In fact, noncentral contact forces act at the contact point, namely at a distance of the radius from the centers of the particles. This leads to application of moments and thus initiation of rotation of the particles. The rotational degrees of freedom of the individual beads have to be considered, and this enriches the elastic-wave propagation, including the

possibility of transverse-rotational elastic waves. Experimentally, the role of rotations has been revealed in only a few reported studies [13–16].

In recent decades, the use of magnetic elements to control wave propagation in discrete systems has received growing interest. The nonlinear magnetic potential between the particles has been explored via repelling magnetic oscillators, showing the existence of solitary waves [17], chaotic behavior [18], moving breathers [19], and second-harmonic generation [20]. A magnetic field has been also used as an external stimulus in order to introduce contactless tunability of band-gap structure [21–25]. In our case, we use an appropriately designed external magnetic field in order to provide local stable attracting forces between the adjacent elastic particles. In this way, we can avoid the application of an external load using mechanical boundaries, a technique used a lot in granular-chain experiments.

In particular, the magnetic field is induced by a linear array of permanent neodymium-alloy ($Nd_2Fe_{14}B$) magnets located in a holder at a given distance from the granular chain. The steel particles used here are ferromagnetic and thus can be strongly magnetized in the presence of a magnetic field, leading to attractive forces between them. A schematic illustration of the magnetogranular phononic crystal is shown in Fig. 1.

This setup offers the advantages of straightforward construction and noncontact tunability via external magnetic fields [15], since a modification of the magnetic

_____
[*]florian.allein@univ-lemans.fr
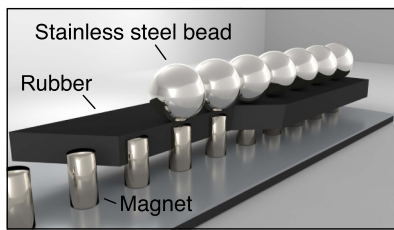[†]georgiostheocharis@gmail.com

FIG. 1. Schematic illustration of the magnetogranular phononic crystal, where a magnetic field, created by the permanent magnets, induces attractive forces between the particles.

field strength allows tuning of the interparticle forces and consequently of the dynamic response of the granular crystal. In addition, the spatial design of the external magnetic field enables the construction of many complex waveguide geometries such as L-shaped, Y-shaped, or curved granular networks and can be easily extended to two-dimensional structures such as square or honeycomb lattices [16], for example. Envisioning a tailoring of the interparticle forces together with the waveguide geometry could lead to appealing functionalities such as routing of waves in specific channels along with frequency filtering depending on the polarization of the wave. Another advantage of the setup is the presence of free boundaries. In a similar magnetogranular (graphene) system [16], this led to the experimental observation of edge modes in free armchair and zigzag boundaries.

In this paper, we report on elastic-wave propagation in a one-dimensional magnetogranular phononic crystal with both longitudinal and transverse polarizations. The complete propagation of longitudinal and transverse-rotational waves is analytically, numerically, and experimentally analyzed. After a description of the modeling of the granular chain and its dynamical equations of motion, we first investigate the linear dynamical regime, where we present the theoretical and experimental dispersion band diagram of such a system considering normal, shear, and rotational motion of the particles. By direct comparison of spatiotemporal measurements using a scanning laser-based probe at the individual-particle level and numerical simulations, we estimate the precompression force and the losses for different polarizations of propagating waves (i.e., for propagation of longitudinal and transverse-rotational waves). We analyze the propagation of pulses and harmonic waves for these two wave types. In the second part of the paper, we turn our attention to the theoretical and experimental investigation of second-harmonic generation with longitudinally polarized waves. We analyze beating in the amplitude of the second harmonic [26,27] of longitudinal waves, considering dissipation and reflection from boundaries. Finally, we investigate the propagation of transverse-rotational waves in the weakly nonlinear regime, in particular under oblique excitation. In this case,

a longitudinal wave is also excited and is nonlinearly coupled to the transverse-rotational wave.

II. MODELING OF GRANULAR CHAINS

A. Description of the contact between spherical particles

We start by reviewing the basic contact laws for normal and tangential loading of two elastic spherical particles. The two spheres, under the action of a normal static load F_0, deform at the point of first contact so that they touch over an area which is significantly smaller than the radii of the two spheres. The normal force between two spheres is given by the following relation using the Hertz theory [1]:

$$F_N = A \left[\delta_0 + \Delta_N \right]_+^{3/2}. \tag{1}$$

The coefficient A depends on the material and geometric properties of the particles. For the case of two identical spheres, $A = E\sqrt{2R}/[3(1 - v^2)]$, where R, E, and v are the radius of the bead, the Young's modulus, and the Poisson's ratio, respectively. δ_0 denotes the static overlap between the two particles and can be written as $\delta_0 = (F_0/A)^{2/3}$, while Δ_N denotes the normal relative displacements of the particles. The symbol $[s]_+$ means that there is no force between the particles when they are separated (a gap is opened); for $s < 0$, the bracket $[s]$ takes the value 0, and for $s > 0$, the bracket takes the value s.

The shear force between two spheres is obtained by applying the Hertz-Mindlin theory [28]. This theory provides a relation between the relative transverse displacement and the elastic shear restoring force. Assuming that there is no sliding at the contact, the shear force, F_S, can be expressed as a function of the transverse and normal displacements Δ_S and Δ_N, respectively, as

$$F_S = B\Delta_S \left[\delta_0 + \Delta_N \right]_+^{1/2}, \tag{2}$$

where the coefficient B also depends on the properties of the particles and is defined for two identical particles as $B = E\sqrt{2R}/[(2 - v)(1 + v)]$. We can observe that the shear force varies linearly with the transverse displacements Δ_S and nonlinearly with the normal displacements Δ_N.

The shear force results in noncentral forces at the local contacts, at a distance equal to the radius of the spherical particles. Thus these forces also induce moments in the finite-size particles and, as a consequence, the spheres are rotated. When the rotational degrees of freedom are activated, one has to take into account two more possible mechanical-contact couplings: (i) the torsional contact coupling, which is due to the resistance of the local contact to relative rotations of the beads about the axis connecting their centers; and (ii) the bending contact coupling, which is due to the resistance of the contact of the particles to
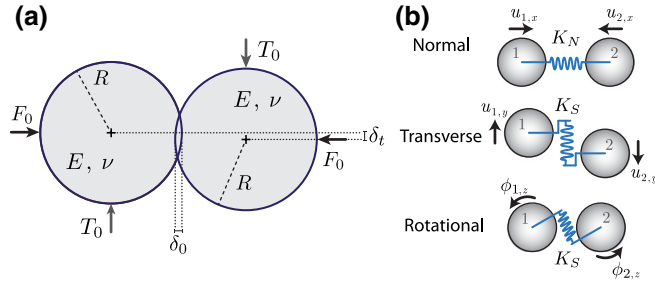
(a)

(b)

FIG. 2. (a) Schematic illustration of the contact between two elastic particles subjected to normal forces F_0 and transverse forces T_0. (b) Schematic presentation of the normal, shear, and rotational interactions.

rolling. Figure 2 depicts the contact between two elastic particles subjected to normal and transverse forces, along with a schematic presentation of the linear couplings taken into account in the modeling.

B. Equations of motion

We now consider a one-dimensional chain consisting of spherical particles in contact. The dynamics of the chain can be significantly simplified in the quasistatic regime, namely when the frequency range under consideration is considerably less than the frequencies of the individual particle resonances. In that case, the granular chain can be modeled as a system of rigid masses linked by four types of spring to account for the normal, shear, torsional, and bending contact couplings. However, in the case of nonconsolidated granular crystals, the torsional and bending rigidities are much smaller than the shear and normal rigidities, respectively [29,30]. Thus, these kinds of interactions contribute only to the very low-frequency dynamics of the system and are neglected in this paper.

With these approximations, and assuming the above-mentioned normal and shear contact laws, the nonlinear dynamics of the granular chain can be described by the following set of differential equations:

$$m\ddot{u}_{n,x} = A\left[\delta_0 + \Delta_{N(n)}\right]_+^{3/2}$$
$$- A\left[\delta_0 + \Delta_{N(n+1)}\right]_+^{3/2}, \qquad (3a)$$

$$m\ddot{u}_{n,y} = B\Delta_{S(n)}\left[\delta_0 + \Delta_{N(n)}\right]_+^{1/2}$$
$$- B\Delta_{S(n+1)}\left[\delta_0 + \Delta_{N(n+1)}\right]_+^{1/2}, \qquad (3b)$$

$$I\ddot{\phi}_{n,z} = -RB\Delta_{S(n)}\left[\delta_0 + \Delta_{N(n)}\right]_+^{1/2}$$
$$- RB\Delta_{S(n+1)}\left[\delta_0 + \Delta_{N(n+1)}\right]_+^{1/2}, \qquad (3c)$$

where n is the particle number, m is the mass of a spherical particle, defined by $m = \frac{4}{3}\pi R^3 \rho$, with ρ the density of

the material, $I = (2/5)mR^2$ is the moment of inertia for a homogeneous sphere, and u_n and ϕ_n are the displacement and rotation, respectively, from the equilibrium position of the nth particle.

The spring elongations corresponding to the relative displacements between the nth particle and its neighboring particles at the contact point are denoted by $\Delta_{N(\cdot)}$ and $\Delta_{S(\cdot)}$ for the normal and shear interactions, respectively, and are given explicitly by

$$\Delta_{N(n)} = u_{n-1,x} - u_{n,x}, \qquad (4a)$$
$$\Delta_{S(n)} = u_{n-1,y} - u_{n,y} + R(\phi_{n-1,z} + \phi_{n,z}). \qquad (4b)$$

C. Analytical dispersion relation

Linearization of Eq. (3), namely assuming that the dynamic relative displacements are much smaller than the static overlap ($\Delta_N/\delta_0 \ll 1$), leads to two decoupled linear sets of motions, namely a longitudinal motion $L(u_x)$ with a displacement along the x axis and a transverse-rotational motion $TR(u_y, \phi_z)$ with a displacement along the y axis and a rotation around the z axis. We can define the linearized rigidities $K_N = (3/2)A\delta_0^{1/2}$ and $K_S = B\delta_0^{1/2}$ for the normal and shear interactions, respectively.

The existence of longitudinal and transverse-rotational modes has been theoretically predicted [31] and experimentally observed [15]. The dispersion curves of such a system are presented in Fig. 3(a) assuming an infinite granular chain.

We can observe that there are two TR propagating bands. The first one corresponds to floppy modes, namely modes with zero frequency for all wave numbers in the Brillouin zone. This comes from an exact counterbalance between rotational and transverse motions, resulting in no elongation of the effective shear springs. The role of these modes in isostatic lattices, and their connection with mechanical instability, has been recently investigated [32,33]. However, if one takes into account the bending rigidity (ignored in this paper), instead of zero-frequency modes one gets propagating modes at very small frequencies, up to 100 Hz, due to the small value of the bending rigidity of granular contacts.

The percentages of the transverse (u) and rotational (ϕ) components in the upper branch TR are displayed in Fig. 3(b) as a function of the frequency. One can see that the transverse (rotation) component is reduced (increased) as the frequency increases. Interestingly, the TR normal modes at $k = 0$ and $k = \pi/a$, shown in Figs. 3(c) and 3(d), respectively, are purely rotational and transverse, respectively. For the mode at $k = 0$, Fig. 3(c), we can observe that the spheres are all rotating in the same direction, and thus the transverse motion is not activated. At $k = \pi/a$, Fig. 3(d), the adjacent particles are moving in opposite directions, which leads to a compensation of the rotational motion, and then the rotational part is equal to zero.
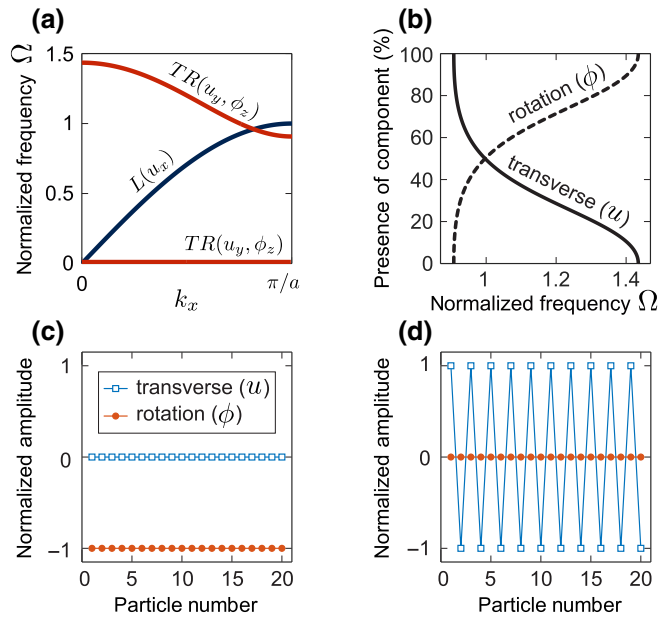
FIG. 3. (a) Dispersion relation for an infinite granular chain. The cyclic frequency ω is normalized by the linear longitudinal cutoff cyclic frequency $\omega_c = \sqrt{4K_N/m}$, namely $\Omega = \omega/\omega_c$, and the lattice constant is $a = 2R$. (b) Relative amplitude (expressed as a percentage) of transverse motion (u) and rotation (ϕ) in the upper TR branch as a function of the normalized frequency. (c),(d) Normal mode of the upper TR branch for a chain of 20 beads, assuming periodic boundary conditions at (c) $k = 0$ and (d) $k = \pi/a$, for the transverse and rotational components.

III. EXPERIMENTAL DISPERSION RELATION

A. Experimental setup

We are now interested in the experimental characterization of the dispersion relation. To do so, we make use of the proposed magnetogranular chain setup [15,34]. This consists of stainless-steel spheres (material characteristics $E = 190$ GPa, $\nu = 0.3$, and diameter 15.87 mm) placed on top of a soft rubber substrate with permanent magnets inside it, as depicted in Fig. 1. The magnetic field of the permanent magnets, as designed, induces attractive forces between the spheres. This leads to a stable linear array. Soft rubber is used as a substrate to minimize the coupling between the granular chain and the substrate. The coupling is minimized because of the high impedance contrast between the granular chain and the substrate, which guarantees that the energy leakage from the chain to the substrate is weak. In addition, this weak energy leakage is highly attenuated due to the high viscoelasticity of rubber. We note also that the effective contact stiffness originating from the contact deformation between the spheres and the substrate, $\tilde{K}_s$, is clearly smaller than the shear contact stiffnesses between the spheres, $\tilde{K}_s/K_S = 0.006$ (assuming the following elastic properties for the substrate: $\nu_s = 0.48$ and $E_s = 2.1$ MPa). In comparison, the ratio of the shear

and normal stiffnesses between the beads is $K_N/K_S = 1.21$. The wave dynamics due to the interaction between the spheres and the substrate will affect low frequencies (up to 300 Hz), which are much lower than the frequencies studied here. Thus, we ignore this elastic mechanical coupling and approximate the granular chain as a freestanding chain, but the losses stemming from the contact with the soft substrate cannot be neglected. The experimental setup is presented in Fig. 4(b).

The chain is driven from one side using a sphere which is glued to a Panametrics V3052 longitudinal transducer or to a Panametrics V1548 shear transducer. For oblique excitation of the chain, we mount the longitudinal transducer on a rotating z axis, to control the angle of excitation θ. For $\theta = 0°$, the transducer provides pure longitudinal excitations in the chain, while for $\theta = 90°$ it provides pure transverse excitations. We note here that without using an accurate positioning system, there is an uncertainty in the exact value of θ. Thus, when we drive the chain at an angle θ, we consider this as a free parameter which is fitted by the direct comparison with numerical simulations. For detection, we use two Polytec OFV-503 laser vibrometers. We measure the velocity of each particle during wave propagation along the x and y directions at the same time. The first laser vibrometer is placed on the side of the chain at a given angle φ, and we project the velocity obtained along the x axis by use of the basic trigonometric formula $v_x = v(\varphi)/\cos(\varphi)$. The second vibrometer is placed above
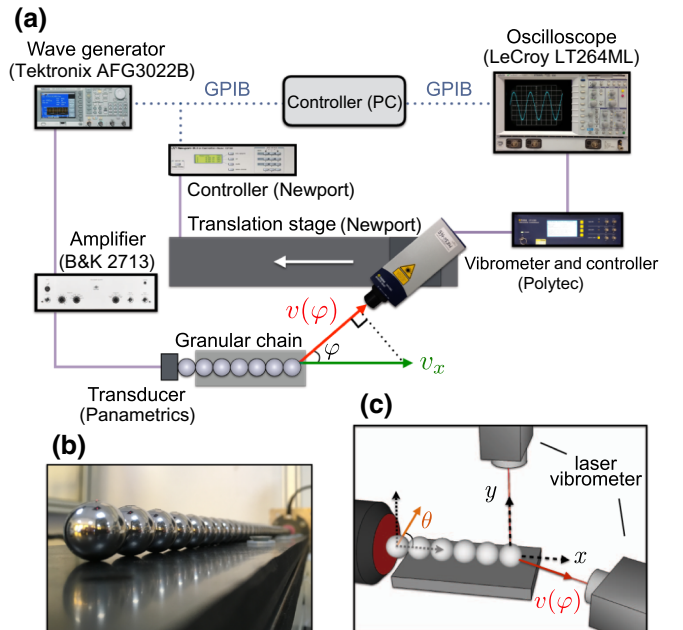

FIG. 4. (a) Diagram of the instrumentation. (b) Photograph of the 38-bead chain on top of the rubber substrate, with permanent magnets inside it. (c) Schematic illustration of the measurement positions of the laser vibrometers.

the granular chain and measures the velocity along the y direction without an angle. A diagram of the experimental instrumentation is presented in Fig. 4(a), and a schematic representation of the measurement positions is shown in Fig. 4(c).

In order to derive the experimental dispersion relation, we choose a "haversine" signal, which can be analytically described as one period of $\sin^2(\xi/2)$, as presented in Fig. 5(a). The frequency of the "haversine" cycle is chosen as 20 kHz, and the frequency bandwidth of the excitation is shown in Fig. 5(b). After measuring the displacements of each particle in the chain, we apply a two dimensional (space-time) Fourier transformation to the recorded signals, which leads to the experimental dispersion curves.
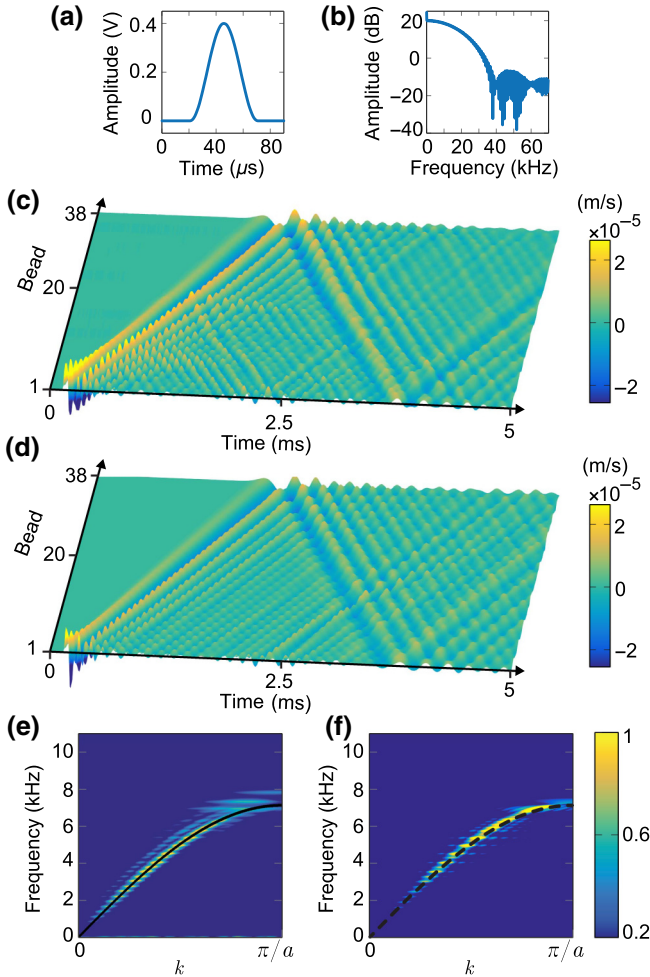

(a)

(b)

(c)

(d)

(e)

(f)

FIG. 5. One period of the "haversine" electric-signal excitation used to derive the dispersion curves, in (a) temporal and (b) frequency domain. (c) Experimental and (d) numerical velocities ($\dot{u}_x$) for longitudinal-wave propagation of a pulse as a function of time on a chain of 38 beads. (e) Experimental and (f) numerical dispersion curves with $F_0 = 1.8$ N and $\tau_x = 2.4$ ms ($\delta_0 = 325$ nm). Analytical dispersion curves are superimposed.

B. Modeling of driven-damped dynamics

For a direct comparison of the experiments with simulations, we consider driven and free boundary conditions for the first and the last particle, respectively. In addition, to account for the wave attenuation during propagation, a linear viscous on-site dissipation is used, with a polarization-dependent decay time τ. This dissipative model highlights the fact that most of the losses stem from the contact between the particles and the soft substrate and can be interpreted as friction occurring at this contact. Such a model of dissipation has been proven to describe experiments on granular chains in previous work well; see for example Refs. [10,35–37]. Different approaches, which account for linear viscoelastic behavior of the elastic and shear moduli of the particles (see for example Refs. [38–43] and references therein), have been proposed and could be also considered in our case. A more systematic way to model the dissipative mechanism in our setup will be considered in future work. Despite the simplicity of our dissipative model, our formulation allows good agreement with the experimental results while keeping the great simplicity of implementation of this formulation.

Under these assumptions, the system is described by the following set of differential equations:

$$m\ddot{u}_{n,x} = A\left[\delta_0 + \Delta_{N(n)}\right]_+^{3/2}$$
$$- A\left[\delta_0 + \Delta_{N(n+1)}\right]_+^{3/2} - m\dot{u}_{n,x}/\tau_x, \quad (5a)$$

$$m\ddot{u}_{n,y} = B\Delta_{S(n)}\left[\delta_0 + \Delta_{N(n)}\right]_+^{1/2}$$
$$- B\Delta_{S(n+1)}\left[\delta_0 + \Delta_{N(n+1)}\right]_+^{1/2}$$
$$- m(\dot{u}_{n,y}/\tau_y - R\dot{\phi}_{n,z}/\tau_z), \quad (5b)$$

$$I\ddot{\phi}_{n,z} = -RB\Delta_{S(n)}\left[\delta_0 + \Delta_{N(n)}\right]_+^{1/2}$$
$$- RB\Delta_{S(n+1)}\left[\delta_0 + \Delta_{N(n+1)}\right]_+^{1/2}$$
$$- mR(R\dot{\phi}_{n,z}/\tau_z - \dot{u}_{n,y}/\tau_y). \quad (5c)$$

The spring elongations, describing the relative displacements between the nth particle and its neighboring particles, are denoted by $\Delta_{N(\cdot)}$ and $\Delta_{S(\cdot)}$ for the normal and shear interaction, respectively, and are given explicitly by

$$\Delta_{N(1)} = u_{\text{act},x} - u_{1,x}, \quad (6a)$$

$$\Delta_{N(i)} = u_{i-1,x} - u_{i,x}, \quad (6b)$$

$$\Delta_{N(N+1)} = 0, \quad (6c)$$

$$\Delta_{S(1)} = u_{\text{act},y} - u_{1,y} + R(\phi_{\text{act},z} + \phi_{1,z}), \quad (6d)$$

$$\Delta_{S(i)} = u_{i-1,y} - u_{i,y} + R(\phi_{i-1,z} + \phi_{i,z}), \quad (6e)$$

$$\Delta_{S(N+1)} = 0, \quad (6f)$$

with $i = 2, \ldots, N$. The driver displacement is denoted by u_{act}. Note that we consider only displacement (not rotational) excitations, as in the experiments. In particular, the experimental signal recorded at the transducer is used as a numerical driver for a direct comparison between the experiments and numerical simulations. From this direct comparison, we observe a good match in the wave propagation attenuation, assuming identical values for the transverse and rotational dissipative terms, namely $\tau_y = \tau_z$. Thereafter, we consider a single value for the dissipative terms of the *TR* waves and denote it by τ_y only.

The set of differential equations in Eqs. (5) is solved by using a fourth-order Runge-Kutta method. From a comparison of the experimental results and simulations, we estimate the precompressional force F_0, the wave attenuation coefficients $\tau_{x,y}$, and the angle of excitation θ. We note here that our setup is sensitive to the exact arrangement or misalignment of the spheres. Because after each series of experiments the spheres are taken off the setup to be cleaned, and then they are replaced for a new series of measurements, they are not exactly at the same positions each time, and this leads to small differences in the precompression. Thus, the precompression force F_0 has to be slightly readjusted and recalculated from experiment to experiment. Experimentally, we also estimate the precompression force between two particles by measuring the pulling force required to separate these particles with a dynamometer. Considering stainless-steel beads of diameter 15.87 mm placed 1.5 mm from the top of cylindrical magnets with a remanent magnetization $B = 1.37$ T, we obtain an estimate of the precompression force between the spheres of $F_0 = 1.5 \pm 0.15$ N.

C. Results

Figures 5(c)–5(f) present experimental and numerical results for longitudinal-wave propagation and the dispersion curve.

For the numerical simulations, we use $F_0 = 1.8$ N, $\tau_x = 2.4$ ms, and $\theta = 0°$. In the spatiotemporal results presented in Figs. 5(c) and 5(d), we can observe good agreement between the experiments and numerics. In addition, in the experiments we also observe a scattered wave initiated by particle 20. This feature is not observed in the numerics, where a perfectly aligned chain is considered. Thus, we believe that this scattering is due to the presence of a defect in the chain due to a modification of the precompression force and/or a misalignment of particle 20. In Figs. 5(e) and 5(f), we present the linear amplitude of the two-dimensional Fourier transform normalized by the maximum amplitude. The theoretical dispersion relation is also superimposed. It should be noted that at very low frequency, the smaller displacement amplitude comes from the experimental transducer, which is not efficient at these low frequencies.
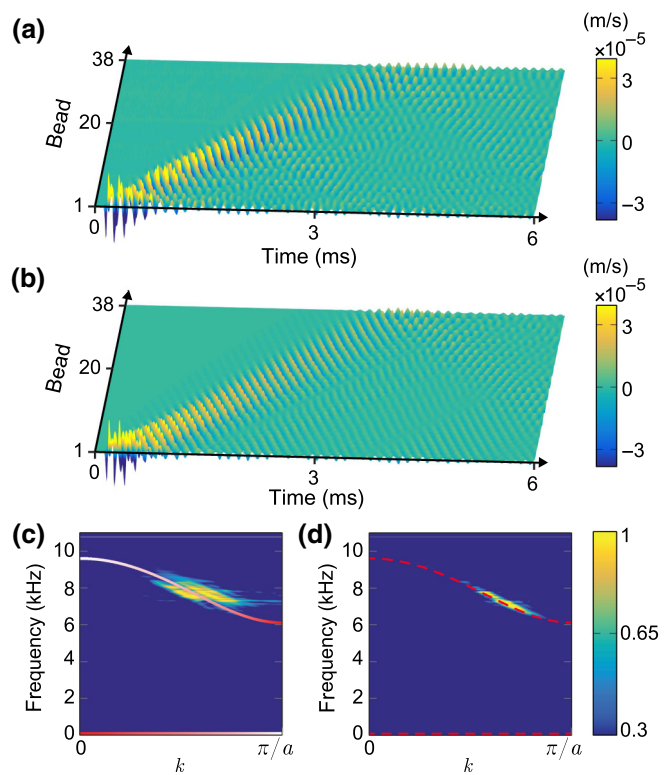

FIG. 6. (a) Experimental and (b) numerical velocities ($\dot{u}_y$) for transverse-wave propagation of a pulse as a function of time in a chain of 38 beads. (c) Experimental and (d) numerical dispersion curves with $F_0 = 1.4$ N and $\tau_y = 2$ ms. Analytical dispersion curves are superimposed.

Let us now examine the propagation of coupled transverse-rotational waves, obtained by driving the chain vertically with a shear transducer (Panametrics V1548), and measured in the same direction. The results are shown in Fig. 6, where for the numerical simulations we use the values $F_0 = 1.4$ N, $\tau_y = 2$ ms, and $\theta = 90°$.

Looking at the temporal evolution of the propagation of a *TR* pulse in Figs. 6(a) and 6(b), we observe a characteristic difference in the propagation in comparison with the *L* branch. The spatiotemporal pattern of the wave propagation in the *TR* branch is different from that for the *L* branch due to the opposite signs of the group and phase velocities. We note that in order to fit the experimental results, the dissipation has to be larger for the *TR* than for the *L* polarization of the propagation ($\tau_y = 2$ ms, $\tau_x = 2.4$ ms). This increase in losses is expected because during the propagation of *TR*-polarized waves, the spheres are under transient oscillating loading by the soft viscoelastic substrate. Finally, from the temporal evolution of the signal, we observe again some scattering as the signal propagates along the chain, indicating again the influence of small misalignments of the spheres.

Figure 6(c) shows the experimental dispersion curve. The superimposed line with a color scale shows the

theoretical prediction for the u_y component, where a white color denotes the absence of the u_y component while a red color denotes 100% of that component. Note that the percentage of each motion is explicitly presented in Fig. 3(b). The first *TR* branch close to zero frequency (as mentioned above, experimentally we expect this branch not to be exactly at zero but at very small frequencies) is not measured, because the experimental transducer cannot transmit enough energy at this frequency. Regarding the second, upper *TR* branch, with increasing frequency, the rotational motion becomes more and more dominant. In fact, both in the experiments and in the numerics, the upper part of the branch has a very weak amplitude, in contrast with the lower part. It should be noted that close to $k = \pi/a$, the experimental results fail to describe the theoretical branch. An explanation for the absence of this part of the dispersion curve may be the very small values of the group velocity close to $k = \pi/a$. As has been demonstrated in Ref. [44,45], slow sound propagation leads to enhanced damping.

IV. HARMONIC WAVES

A. Near-linear regime

In the previous section, we derive the dispersion relation experimentally. In this subsection, we present in more detail the near-linear propagation ($\Delta_N/\delta_0 \ll 1$) of harmonic waves in magnetogranular chains, both with longitudinal and with transverse-rotational polarization.

The equations of motion in the near-linear regime are given by

$$m\ddot{u}_{n,x} = K_N \left[\Delta_{N(n)} - \Delta_{N(n+1)} \right] - m\dot{u}_{n,x}/\tau_x, \quad (7a)$$

$$m\ddot{u}_{n,y} = K_S \left[\Delta_{S(n)} - \Delta_{S(n+1)} \right]$$
$$- m(\dot{u}_{n,y} - R\dot{\phi}_{n,z})/\tau_y, \quad (7b)$$

$$I\ddot{\phi}_{n,z} = -RK_S \left[\Delta_{S(n)} + \Delta_{S(n+1)} \right]$$
$$- mR(R\dot{\phi}_{n,z} - \dot{u}_{n,y})/\tau_y. \quad (7c)$$

As mentioned above, in the linear regime the longitudinal motion (u_x) is decoupled from the transverse-rotational (u_y, ϕ_z) motions.

The granular chain is excited obliquely from one side using a Panametrics V3052 longitudinal transducer. An example of the numerical and experimental spatiotemporal evolution of the particle velocities is presented in Fig. 7 for a chain of 38 spheres and an excitation angle $\theta = 55°$. A harmonic sine-wave excitation is used with a frequency of 3 kHz, corresponding to $\Omega = \omega/\omega_c = 0.42$. Figure 7(a) presents the experimental results measured with a laser sensitive to displacement along the x direction.
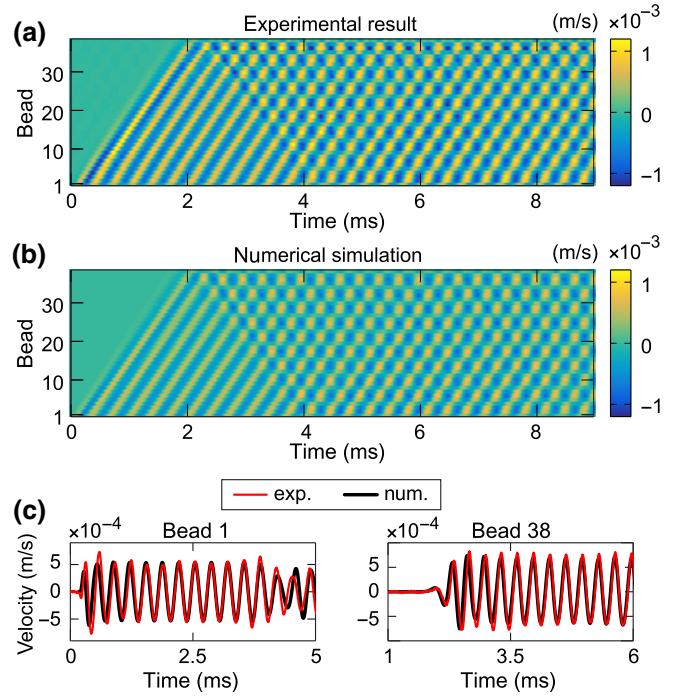

FIG. 7. (a) Experimental spatiotemporal diagram of the velocity $\dot{u}_x$ of the particles during the propagation of a sine wave with a frequency of 3 kHz ($\omega/\omega_c = 0.42$). (b) Numerical spatiotemporal diagram of the velocity $\dot{u}_x$ with $F_0 = 1.55$ N and $\tau_x = 2.4$ ms. (c) Velocity $\dot{u}_x$ as a function of time for (left) the first bead and (right) the last bead of the chain.

By fitting the precompression force to $F_0 = 1.55$ N and the decay time for longitudinal excitations to $\tau_x = 2.4$ ms, good agreement is found between the experiments [Fig. 7(a)] and the numerical simulations [Fig. 7(b)]. Note that the dissipation parameter for the propagation of an *L* sine wave is identical to the value obtained using pulse-wave excitation. From the theoretical predictions, a harmonic wave with a frequency $\Omega = 0.42$ is a propagating wave in the longitudinal case and evanescent in the transverse-rotational case. In fact, we can clearly observe that for the motion directed along the x axis, the harmonic wave propagates to the end of the chain, where it is reflected. After a certain time, a steady state is obtained. The ratio between the maximum amplitude received by the vertical laser and that received by the horizontal one is equal to 2 for the first bead and 0.017 for the 15th bead in the chain. In other words, the amplitude in the transverse direction of propagation is two orders smaller than that in the longitudinal direction at the 15th site, which indicates that the wave is evanescent.

We now excite the chain at the same angle of excitation but with a sine wave of frequency 8 kHz ($\omega/\omega_c = 1.13$). This frequency results in propagating waves for the transverse-rotational motion and evanescent waves for the longitudinal motion. Figure 8 presents the experimental
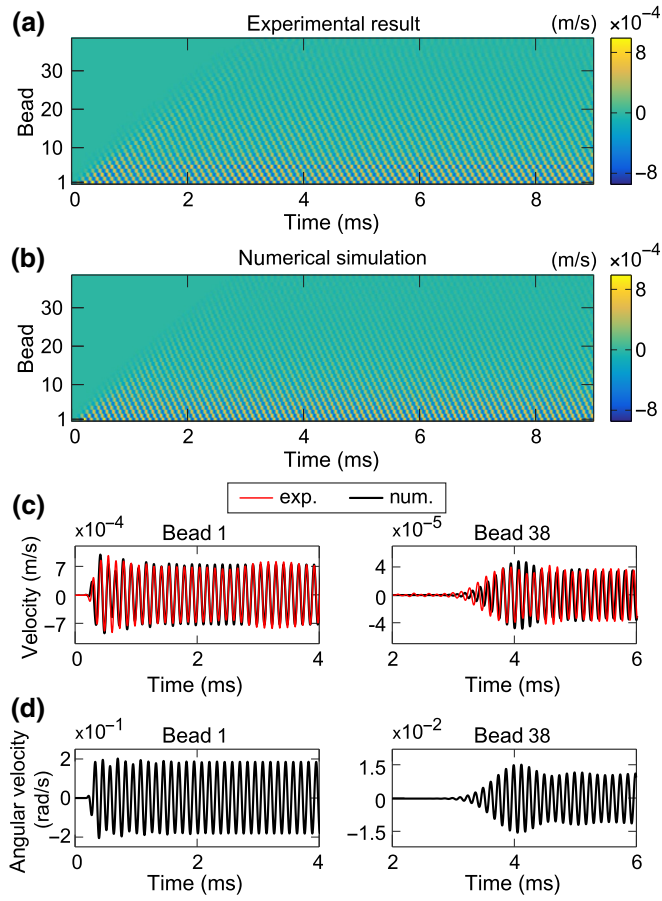
(a) Experimental result

(b) Numerical simulation

(c)

(d)

FIG. 8. (a) Experimental spatiotemporal diagram of the velocity $\dot{u}_y$ of the particles during the propagation of a sine wave with a central frequency of 8 kHz. (b) Transverse part of the numerical spatiotemporal diagram with $F_0 = 1.55$ N and $\tau_y = 0.93$ ms. (c) Velocity $\dot{u}_y$ and (d) angular velocity $\dot{\phi}_z$ as a function of time for (left) the first bead and (right) the last bead of the chain.

and numerical spatiotemporal evolution of the particle velocities for transverse-rotational propagation in this configuration.

Qualitatively good agreement is found between the experiments and numerics. Regarding the temporal signal measured for the first and the last particle [Fig. 8(c)], we find good agreement with the numerics. To complete the description of transverse-rotational-wave propagation, the rotational part obtained from the numerics is shown in Fig. 8(d). It should be noted that the laser vibrometer is not sensitive to rotation; thus, experimentally, only transverse displacements are recorded. As we can see, although the chain is excited by a purely transverse motion, rotational motion is also excited. As mentioned in the previous section, the system supports coupled transverse-rotational waves. The percentage of rotational motion in the coupled *TR* propagating wave depends on the frequency. For example, for the case of 8 kHz studied here, the theory predicts 65% of rotation, as presented in Fig. 3(b),

which is confirmed by the simulations. In order to fit the experimental results for *TR* propagation, the precompression is now $F_0 = 1.55$ N, which is identical to that for *L* propagation. We note that the experiments on *TR* wave propagation are done with the same configuration as the previous experiments on *L* propagation.

These first results show that our setup, in the linear regime, is well described by the proposed model and that all our approximations are valid. In addition, we show that the precompression is identical regardless of the polarization of the motion, namely longitudinal or transverse motion, as long as we are referring to the same configuration. Finally, as has been already commented on for the dispersion-relation experiments, the effective dissipation is larger during *TR* propagation than during *L* propagation.

B. Weakly nonlinear regime

In this section, we present a study of wave propagation in the weakly nonlinear regime both for the longitudinal and for the transverse-rotational polarization.

The equations of motion in the weakly nonlinear regime are obtained by Taylor expansion of Eqs. (5) and keeping terms up to quadratic order. Thus, the following equations are obtained:

$$m\ddot{u}_{n,x} = K_N \left[\Delta_{N(n)} - \Delta_{N(n+1)} \right] - m\dot{u}_{n,x}/\tau_x$$
$$+ \frac{K_3}{2} \left[\left(\Delta_{N(n)} \right)^2 - \left(\Delta_{N(n+1)} \right)^2 \right], \quad (8a)$$

$$m\ddot{u}_{n,y} = K_S \left[\Delta_{S(n)} - \Delta_{S(n+1)} \right]$$
$$+ K_{S3} \left[\Delta_{S(n)}\Delta_{N(n)} - \Delta_{S(n+1)}\Delta_{N(n+1)} \right]$$
$$- m(\dot{u}_{n,y} - R\dot{\phi}_{n,z})/\tau_y, \quad (8b)$$

$$I\ddot{\phi}_{n,z} = -RK_S \left[\Delta_{S(n)} + \Delta_{S(n+1)} \right]$$
$$- RK_{S3} \left[\Delta_{S(n)}\Delta_{N(n)} + \Delta_{S(n+1)}\Delta_{N(n+1)} \right],$$
$$- mR(R\dot{\phi}_{n,z} - \dot{u}_{n,y})/\tau_y. \quad (8c)$$

where $K_3 = (3/4)A\delta_0^{-1/2}$ and $K_{S3} = (1/2)B\delta_0^{-1/2}$. In the weakly nonlinear regime, the transverse and rotational motions are coupled to the longitudinal motion.

1. Longitudinal harmonic waves: theory

We start with the case of purely longitudinally polarized harmonic waves. In this case, Eq. (8a) describes weakly nonlinear longitudinal propagation. The quadratic term results in the generation of harmonics. When harmonics are generated in a dispersive medium, the interaction between the fundamental frequency and the second harmonic is different from that in the nondispersive case.

First, we focus on the regime where the fundamental ω_1 and the second harmonic ω_2 are both located in the propagating band, while the third harmonic is in the forbidden gap, i.e., $\omega_1/\omega_c < 0.5$. In this case, the second harmonic is in the strongly dispersive regime of the dispersion relation. Such a configuration has been theoretically investigated in Ref. [26], considering harmonic generation in a semi-infinite granular system. Second-harmonic generation has been also experimentally and theoretically reported in Ref. [46] in a diatomic magnetogranular chain, assuming some *ad hoc* viscouslike damping (implemented by adding a small imaginary part to the wave number). The authors of Ref. [26] predicted the generation of second harmonics in the presence or absence of dispersion but did not consider the effect of dissipation. Here, we extend the theoretical study by including the effect of viscous dissipation.

Let us first rewrite Eq. (8a) in a dimensionless form by defining a normalized time $t' = \omega_c t$ and normalizing the displacement as $u_n = u_n/u_0$, where u_0 is the characteristic amplitude. Only the motion along the x axis is considered here, and thus the index x is removed to simplify the notation. The dimensionless equations of motion in the weakly nonlinear regime for the longitudinal motion are expressed as

$$(u_n)_{t't'} = \frac{1}{4}(u_{n-1} - 2u_n + u_{n+1}) - \zeta(u_n)_{t'}$$
$$- \frac{\varepsilon}{8}[(u_{n-1} - 2u_n + u_{n+1})(u_{n+1} - u_{n-1})], \quad (9)$$

where $\varepsilon = u_0 K_3/K_N = u_0/(2\delta_0)$ is the nonlinear parameter, $\zeta = 1/(\omega_c \tau)$ is the dissipative parameter, and $(u_n)_{t'}$ and $(u_n)_{t't'}$ are the first and second normalized time derivatives, respectively. In the following development, the prime in t' is removed to simplify the notation. We consider a driven boundary condition for the system such as $u_0(t) = \cos(\Omega t)$.

An approximate solution of Eq. (9) can be obtained by expressing u_n as an asymptotic series in ε, namely

$$u_n(t) = u_n^{(0)}(t) + \varepsilon u_n^{(1)}(t) + O(\varepsilon^2). \quad (10)$$

After substituting Eq. (10) into Eq. (9) and collecting the terms at each order in ε, we obtain the leading-order equations at $O(\epsilon^0)$,

$$(u_n^{(0)})_{tt} - \frac{1}{4}\left(u_{n-1}^{(0)} - 2u_n^{(0)} + u_{n+1}^{(0)}\right) + \zeta(u_n^{(0)})_t = 0, \quad (11)$$

and the equation at the next order $O(\varepsilon)$ is

$$(u_n^{(1)})_{tt} - \frac{1}{4}\left(u_{n-1}^{(1)} - 2u_n^{(1)} + u_{n+1}^{(1)}\right) + \zeta(u_n^{(1)})_t = R', \quad (12)$$

where

$$R' = -\frac{1}{8}\left(u_{n-1}^{(0)} - 2u_n^{(0)} + u_{n+1}^{(0)}\right)\left(u_{n+1}^{(0)} + u_{n-1}^{(0)}\right). \quad (13)$$

Eq. (11) possesses plane-wave solutions of the form

$$u_n^{(0)} = \alpha e^{i[\kappa(\Omega)n - \Omega t]} + c.c., \quad (14)$$

where α is the wave amplitude, c.c. means the complex conjugate, $\kappa = ka$ is the normalized wave number, and κ and Ω satisfy the complex dispersion relation

$$D(\Omega, \kappa) = -\Omega^2 + \sin^2\left(\frac{\kappa}{2}\right) - i\zeta\Omega = 0. \quad (15)$$

When we insert the solution Eq. (14) into Eq. (13), the coefficient R' becomes

$$R' = i \sin^2\left(\frac{\kappa}{2}\right)\sin(\kappa)\alpha^2 e^{i2\theta_n} + c.c., \quad (16)$$

where $\theta_n = \kappa(\Omega)n - \Omega t$.

The solution of Eq. (12) can be written as the sum of a general solution of the homogeneous equation (a free wave at 2Ω) and of a particular solution of the inhomogeneous equations (a forced wave at $2\theta_n$):

$$u_n^{(1)} = A_n' + B'e^{i[\kappa(2\Omega)n - 2\Omega t]} + C'e^{i2\theta_n} + c.c., \quad (17)$$

where A_n' corresponds to a static (zero-frequency) mode, which will be ignored in our study. To obtain the solution of the inhomogeneous part (the forced wave), we assume

$$u_{n,p}^{(1)} = C'e^{i2\theta_n} + c.c., \quad (18)$$

where the index p stands for the *particular* solution. By inserting Eq. (18) into Eq. (12), we can find the amplitude of the forced wave and then that of the free wave, explicitly expressed as

$$C' = -B' = -\frac{i}{8}\cot\left(\frac{\kappa}{2}\right). \quad (19)$$

Finally, the damped solution is

$$u_n \simeq \frac{1}{2}e^{i\theta_n} + \frac{\varepsilon}{4}\cot\left(\frac{\kappa}{2}\right)\sin\left(\frac{\Delta\kappa}{2}n\right)e^{-i(\Delta\kappa/2)n}e^{i2\theta_n} + c.c., \quad (20)$$

where $\Delta\kappa = 2\kappa(\Omega) - \kappa(2\Omega)$ is the wave-number mismatch between the forced and the free contributions to the second harmonic.

Since the forced and free waves have different phase velocities, i.e., $2\kappa(\Omega) \neq \kappa(2\Omega)$, the phase mismatching introduces a beating in space in the amplitude of the second harmonic. In particular, the amplitude of the second harmonic vanishes at the positions n satisfying the following condition:

$$n = \frac{2l\pi}{\Delta\kappa}, \quad (21)$$

where $l \in \mathbb{N}^+$; the amplitude of the second harmonic is maximum when $n = (l\pi)/\Delta\kappa$. In Fig. 9, the analytical and
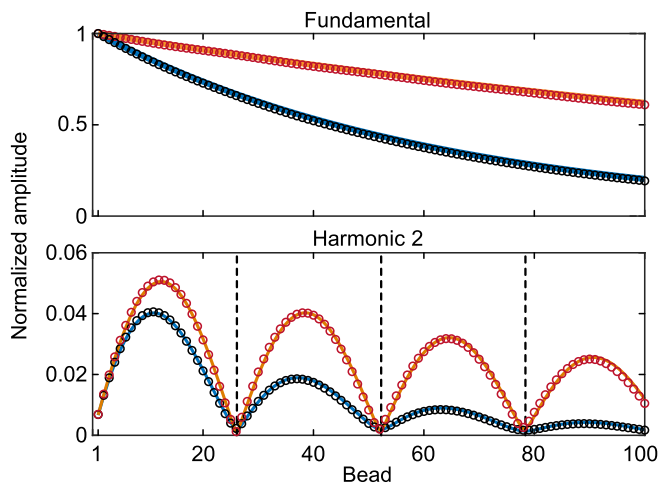
FIG. 9. Comparison of the theoretical result obtained from Eq. (20) (lines) and a numerical simulation of Eq. (8a) (circles). Normalized amplitude of the fundamental (top) and second harmonic (bottom) for $\varepsilon = 0.05$ and $\Omega = 0.41$. The black circles and blue lines correspond to a dissipative term $\tau = 1.5$ ms, while the red circles and orange lines correspond to $\tau = 5$ ms. The vertical dashed lines depict the analytical predictions for the disappearance of the second-harmonic contribution obtained from Eq. (21).
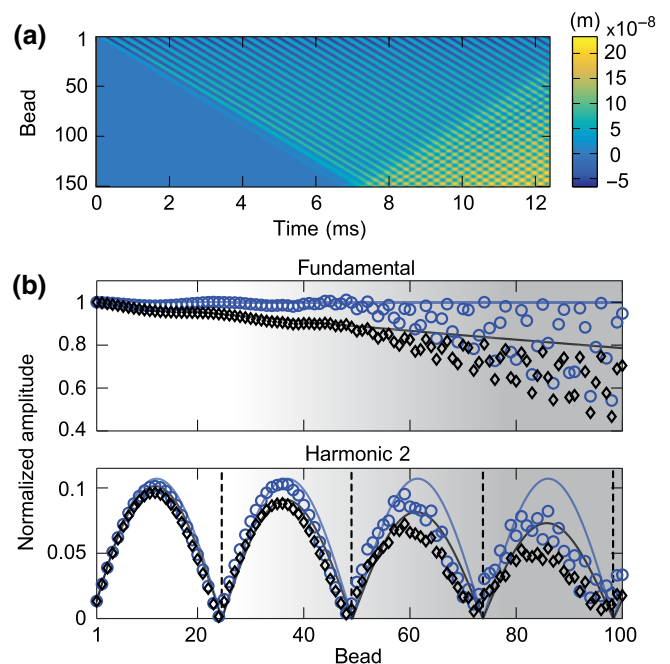

FIG. 10. (a) Spatiotemporal representation of the numerical displacement of the particles as a function of time. (b) Normalized amplitude of the fundamental and second harmonic for $\Omega = 0.42$ and $\varepsilon = 0.1$ when a reflected wave is present. The solid lines correspond to the analytical solution obtained from Eq. (20), and the markers to the numerical results. The blue circles and lines correspond to a lossless case, and the black diamonds and lines to a dissipative case with $\tau = 10$ ms. Gray zones correspond to the presence of reflection during the analysis. The vertical dashed lines are analytical predictions for the disappearance of the second-harmonic contribution obtained from Eq. (21).

numerical results are compared for a driving frequency $\Omega = 0.41$ and a nonlinear parameter $\varepsilon = 0.05$. We present the amplitudes of the fundamental and the second harmonic assuming two values for the damping coefficient: $\tau = 5$ ms and $\tau = 1.5$ ms.

We can see good agreement between the analytical predictions and the numerical results and a clear beating in the amplitude of the second harmonic. In the presence of losses, the amplitude of the fundamental and the maxima of the second harmonic decay as the wave propagates in the chain. We also note that the second harmonic is predicted to vanish at sites $n \approx 26, 52, 78$, which is in good agreement with the numerical results.

The theory for the generation of the second harmonic applied here assumes the absence of reflected waves during the signal analysis. However, due to the finite size of the granular chain, it is useful to study the effect of reflected waves on the beating of the second harmonic. Figure 10(a) presents the spatiotemporal dynamics for a harmonic excitation of amplitude $\Delta_{N(1)}/\delta_0 = 0.19$, corresponding to $\varepsilon = 0.1$ and a driving frequency $\Omega = 0.42$. The chain is composed of 150 particles, and driven-free boundary conditions are considered. We study both the lossless case and the weakly lossy case with $\tau = 10$ ms. From Eq. (21), the amplitude of the second harmonic vanishes at the sites $n \approx 24, 49, 73, 98$.

As presented above, in the presence of losses, the amplitudes of the fundamental and of the second harmonic are reduced as the wave propagates in the chain. The gray

zone in Fig. 10(b) represents the presence of the reflected wave in the analysis. In the absence of the reflected wave, we clearly observe the beating of the second harmonic. On the other hand, the presence of the reflected wave disrupts the beating phenomenon, while eventually, when the reflected part is strong, the beating disappears and the system reaches a nonlinear steady state.

2. Longitudinal harmonic waves: experiments

We now turn our attention in the experimental observation of second-harmonic generation. The experimental setup is identical to that in Fig. 4(a). The velocity of each particle in the 38-bead chain is measured by a laser vibrometer. The chain is driven with a harmonic wave with a short linear ramp in amplitude at the beginning, to avoid the excitation of a wide band of frequencies.

We focus our analysis on the first part of the signal, where there is only a small part of the reflected wave. As commented above, the presence of the reflected wave has to be minimized during the analysis in order to obtain a beating phenomenon in the second harmonic. To do so,
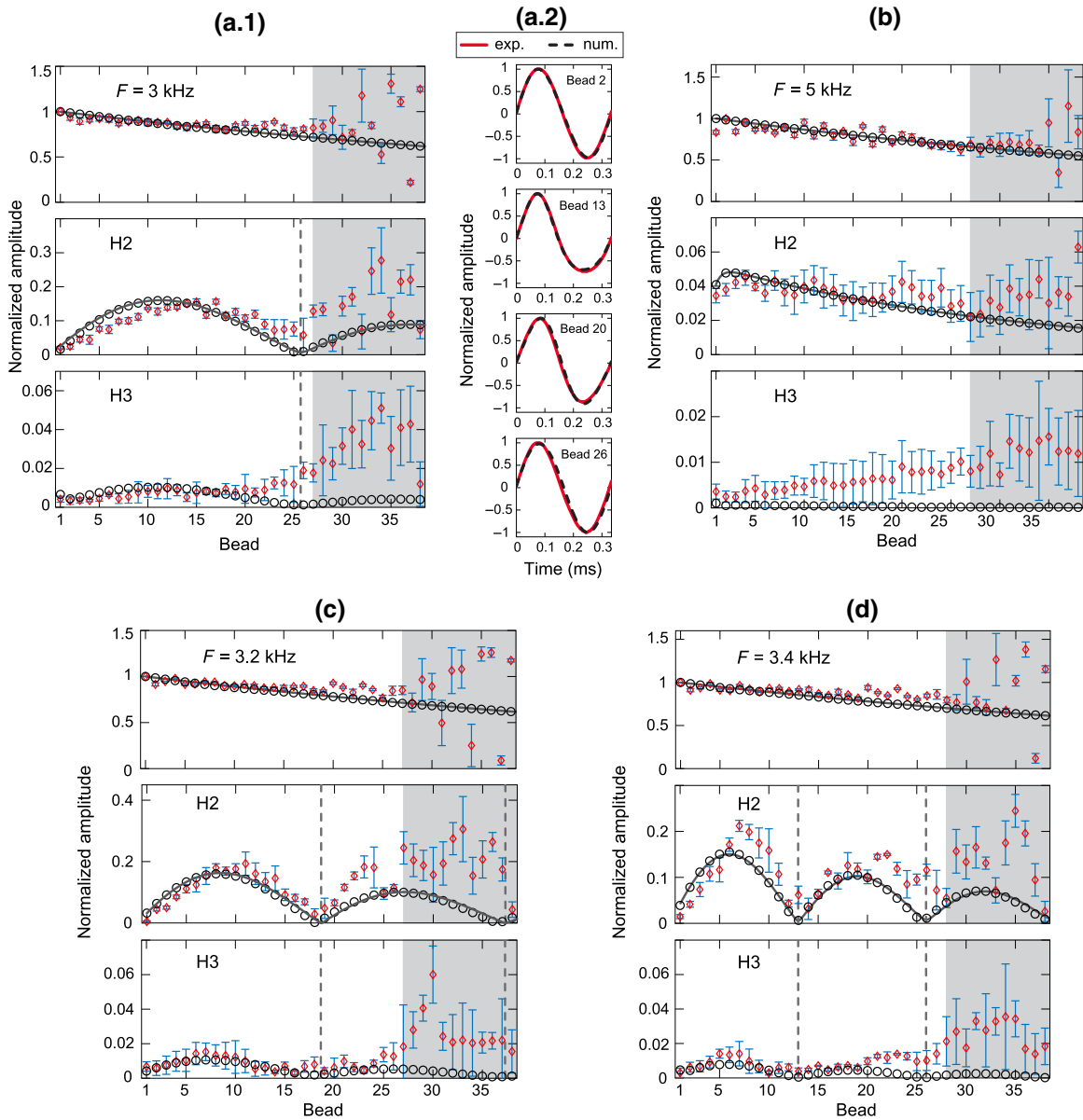
FIG. 11. Experimental, numerical, and analytical harmonic generation for driving frequencies of (a) 3 kHz ($\omega_1/\omega_c = 0.41$), (b) 5 kHz ($\omega_1/\omega_c = 0.69$), (c) 3.2 kHz ($\omega_1/\omega_c = 0.44$), and (d) 3.4 kHz ($\omega_1/\omega_c = 0.47$). The black circles, red diamonds, and solid lines correspond to numerical, experimental, and analytical results, respectively. The vertical dashed lines are given by Eq. (21). Gray zones correspond to the experimental presence of reflection during the analysis.

we take only one period of the signal close to its beginning. Starting the analysis at the first period just after the linear ramp (and repeating this for the two following periods) allows us to get rid of the reflection up to the 27th particle. Numerical simulations are used to fit the precompression and the damping term to the experimental results. The precompression is found to be $F_0 = 1.8$ N, leading to a cutoff frequency of $\omega_c = 2\pi \times 7240$ rad/s, and the damping term is $\tau = 1.9$ ms. Figures 11(a) and 11(b) present the experimental and numerical results for driving fundamental frequencies of 3 kHz ($\omega_1/\omega_c = 0.41$)

and 5 kHz ($\omega_1/\omega_c = 0.69$). The experimental velocity signal recorded at the transducer is used as the driver in the numerical simulation. The maximum of the displacement relative to the static overlap is $\Delta_{N(1)}/\delta_0 = 0.19$, ensuring that we are in the weakly nonlinear regime.

The numerical results presented in Fig. 11 are obtained using a large chain of 238 particles to avoid completely the reflected wave during the analysis. Figure 11(a) depicts the harmonic generation for a driving frequency of 3 kHz. In this case the second harmonic (H2) is inside the propagating band, while the third harmonic (H3) is in the gap. From
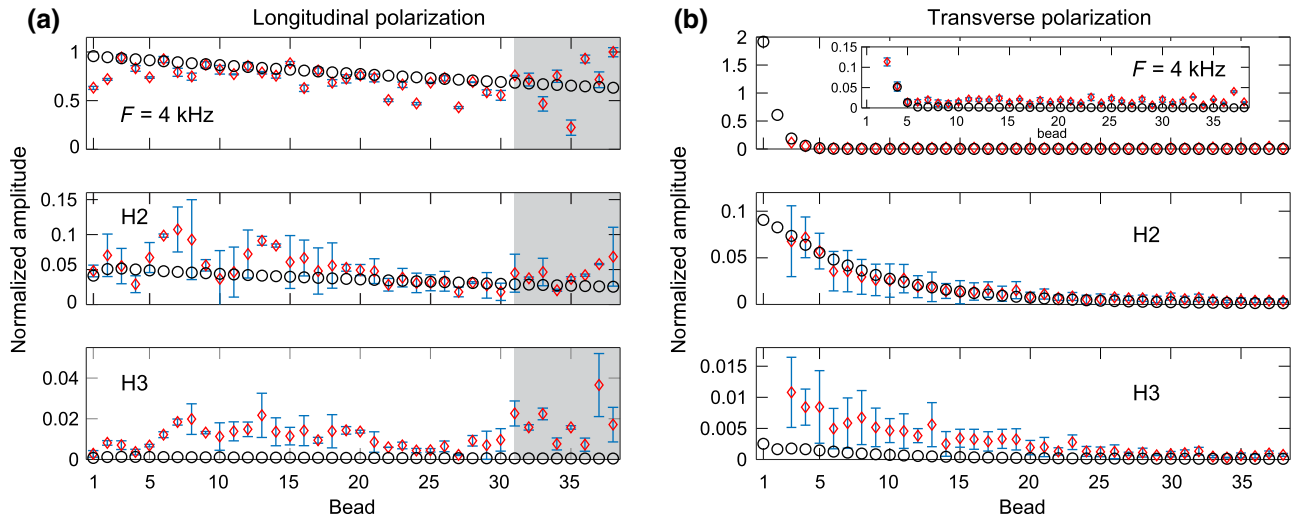
FIG. 12.   Experimental and numerical harmonic generation for a driving frequency of 4 kHz ($\omega_2/\omega_c = 0.58$). The longitudinal polarization (u_x component) and the transverse polarization (u_y component) are presented in (a) and (b), respectively. The black circles correspond to numerics and the red diamonds to experimental results. Gray zones correspond to the experimental presence of reflection during the analysis.

Eq. (21), vanishing of the second harmonic is predicted at the 26th bead, shown by the vertical dashed line. Red diamonds represent the mean value of the frequency amplitude and the error bars correspond to the standard deviation found from the analysis of three periods. In addition, the solid lines represent the analytical predictions of the fundamental and second-harmonic amplitudes.

Looking at the experimental results, when there is no reflected wave (white zone), very good agreement with the numerics is found for the dynamics of the fundamental and the second and third harmonics. In the presence of the reflected wave (gray zone), the experimental beating phenomenon is blurred, and the standard deviation clearly increases in this regime. In Fig. 11(a.2), we compare the experimental and numerical temporal signals at different bead positions during the first beating phenomenon (from particle 1 to particle 26). Excellent agreement between the experiments and simulations is observed in this temporal representation. One can also observe that the maximum distortion of the temporal signal appears at bead 13, where H2 takes its maximum value, while at bead 26, the signal recovers its harmonic form, as at this point we observe the vanishing of H2.

In Fig. 11(b), we present the case where the driving frequency is 5 kHz. In this case the second and third harmonics are in the forbidden band for propagation. Once again, the results are in very good agreement, and the second and third harmonics have a very small amplitude. The experimental data for the second and third harmonics have a bigger standard deviation, due to a small signal-to-noise ratio. Now, we modify the fundamental driving frequency to keep the second harmonic in the propagating band, in order to observe the change in the position of the bead

at which the second harmonic vanishes. Figures 11(c) and 11(d) show the results for fundamental frequencies of $f_1 = 3.2$ kHz ($\omega_1/\omega_c = 0.44$) and $f_1 = 3.4$ kHz ($\omega_1/\omega_c = 0.47$), respectively. From Eq. (21), we expect disappearance of the second-harmonic contribution at beads 19 and 37 for a fundamental frequency of 3.2 kHz and at beads 13 and 26 for 3.4 kHz. The maximum of the displacement relative to the static overlap is kept at $\Delta_{N(1)}/\delta_0 = 0.19$.

It should be noted that in all the numerical analysis, the value of the damping term is $\tau = 1.9$ ms, which is close to the fitted value in the previous section, studying the linear wave propagation. If we consider also the dissipation occurring at the contact between the particles, a viscoelastic model for the dissipation could be more appropriate in the nonlinear regime, such as the model developed in Refs. [41–43], where the interparticle force has a nonconservative contribution proportional to the deformation rate. However, the simplified model that we use captures the nonlinear dynamics well.

3. Transverse-rotational harmonic waves

We now investigate experimentally and numerically the propagation of transverse-rotational waves in the weakly nonlinear regime.

The longitudinal transducer is placed at an angle of θ, which is found to be 65° from a direct comparison with the numerics. An oblique driving is chosen in order to excite both the longitudinal and the transverse directions. We measure the velocity of each particle in the chain with two laser vibrometers as presented in Fig. 4(c). Because of practical issues, the first two particles of the chain cannot be detected by the vertical laser, and thus these two points

are missing in the experimental analysis presented below. The excitation frequency is 4 kHz, and the estimated precompression is $F_0 = 1.4$ N, which leads to $\omega_1/\omega_c = 0.58$ for the fundamental and $\omega_2/\omega_c = 1.16$ for the second harmonic. For this case, the fundamental frequency lies in the propagating band for the longitudinal motion and in the lower band gap for the transverse-rotational motion. The second harmonic is in the gap for the longitudinal motion but in the propagating band for the transverse motion. The excitation amplitude is the same as before, namely that in the experiments studying the longitudinal motion, ensuring a weakly nonlinear response. Finally, the estimated damping coefficients are found to be $\tau_x = 2.5$ ms and $\tau_y = 0.6$ ms.

Figure 12 presents the experimental and numerical results for the amplitude of the harmonics in the chain for (a) the longitudinal and (b) the transverse direction. The amplitudes are normalized by the maximum of the fundamental amplitude in the longitudinal direction.

Looking at the results for the longitudinal direction [Fig. 12(a)], we see that they are in rather good agreement; the second and third harmonics have a small amplitude and decay along the propagation direction due to the dissipation. It should be noted that the second-harmonic frequency is close to the propagating band ($\omega_2/\omega_c = 1.16$), and thus we detect more amplitude in this configuration than in the previous case presented in Fig. 11(b), where the second harmonic is deeper in the gap ($\omega_2/\omega_c = 1.29$). Regarding the results in the transverse direction [Fig. 12(b)], we can observe good agreement between the numerics and the experimental results. We can clearly observe that the fundamental amplitude decays quickly, confirming the evanescent regime at this frequency. The amplitudes of the second and third harmonics decay proportionally to the decay of the forced wave along the propagation direction, as expected from the simulations. We can observe that, due to the stronger dissipation in the transverse direction than in the longitudinal one, there is no clear presence of waves reflected by the free boundary of the chain.

V. CONCLUSION

In this paper, we investigate elastic-wave propagation in a one-dimensional magnetogranular phononic crystal. The complete wave propagation of longitudinal and transverse-rotational waves is analytically, numerically, and experimentally analyzed. The experimental setup is composed of a chain of stainless-steel beads placed inside a designed magnetic field. The latter is induced by a linear array of permanent magnets located in a holder, and is responsible for the creation of attractive forces between the ferromagnetic particles.

In the first part of the paper, the granular chain is excited by short wave packets and continuous harmonic waves in the linear dynamical regime. By direct comparison of spatiotemporal measurements using a scanning laser-based probe and numerical simulations, we estimate the precompression force and the losses for different polarizations of propagating waves (i.e., the propagation of longitudinal and transverse-rotational waves). The losses are approximated by viscous on-site damping in the numerical simulations. Then, we theoretically and experimentally derive the dispersion band diagram of such a system considering normal, shear, and rotational interactions between the particles. The experimental and numerical results are in good agreement. The spatiotemporal measurements also point out the presence of defects in the chain, probably due to misalignment of particles, and highlight the fact that the precompression in the experimental setup is sensitive to the initial positions and alignment of the beads.

In the second part, we extend our study to a theoretical and experimental investigation of second-harmonic generation taking into account the nonlinearities originating from the contact between particles. We analyze the beating in the amplitude of the second harmonic of the longitudinal waves when dissipation and reflection are present. When we consider attenuation during propagation, the amplitude of the second harmonic decreases as a function of depth in the chain, but the sites where the second harmonic disappears are the same as in the lossless case. The scanning measurements reveal clear beating phenomena in the longitudinal polarization for several driving frequencies and are in good agreement with theoretical predictions. Finally, we investigate the propagation of transverse-rotational waves in the weakly nonlinear regime, where the longitudinal motion contributes to the transverse-rotational waves. The experimental and numerical results are still in good agreement.

To conclude, magnetogranular structures offer a perfect experimental testbed for the study of novel wave phenomena and advanced control of elastic-wave propagation in the linear and nonlinear regimes. Taking advantage of an external magnetic field to induce tailorable attractive forces between the particles allows one to design many waveguide networks. Starting from the one-dimensional structure studied here, we can envision the realization of new elastic networks in one or two dimensions having desired functionalities for wave propagation. This includes wave routing in specific channels depending on the wave polarization, spatial confinement of waves at the edges of the structure [16], dynamical tunability, and frequency or mode conversion, for example. The interplay between the structure geometry, wave polarizations, and contactless tunability of the dynamical response [15] offers broad control of elastic-wave propagation. The combination of the features mentioned above and the potential nonlinear response of the granular system leads to richer and enhanced functionalities such as harmonic generation, self-demodulation effects, and nonreciprocity. This study

---

[1] K. L. Johnson, *Contact Mechanics* (Cambridge University Press, 1985).

[2] C. Coste, E. Falcon, and S. Fauve, Solitary waves in a chain of beads under Hertz contact, Phys. Rev. E **56**, 6104 (1997).

[3] S. Job, F. Melo, A. Sokolow, and S. Sen, How Hertzian Solitary Waves Interact with Boundaries in a 1D Granular Medium, Phys. Rev. Lett. **94**, 178002 (2005).

[4] A. Leonard and C. Daraio, Stress Wave Anisotropy in Centered Square Highly Nonlinear Granular Systems, Phys. Rev. Lett. **108**, 214301 (2012).

[5] A. Leonard, F. Fraternali, and C. Daraio, Directional wave propagation in a highly nonlinear square packing of spheres, Exp. Mech. **53**, 327337 (2013).

[6] J. Cabaret, P. Béquin, G. Theocharis, V. Andreev, V. E. Gusev, and V. Tournat, Nonlinear Hysteretic Torsional Waves, Phys. Rev. Lett. **115**, 054301 (2015).

[7] N. Boechler, G. Theocharis, S. Job, P. G. Kevrekidis, Mason A. Porter, and C. Daraio, Discrete Breathers in One-dimensional Diatomic Granular Crystals, Phys. Rev. Lett. **104**, 244302 (2010).

[8] G. Theocharis, M. Kavousanakis, P. G. Kevrekidis, C. Daraio, Mason A. Porter, and I. G. Kevrekidis, Localized breathing modes in granular crystals with defects, Phys. Rev. E **80**, 066601 (2009).

[9] M. A. Porter, P. G. Kevrekidis, and C. Daraio, Granular crystals: Nonlinear dynamics meets materials engineering, Physics Today **68**, 44 (2015).

[10] N. Boechler, G. Theocharis, and C. Daraio, Bifurcation-based acoustic switching and rectification, Nat. Mater. **10**, 665668 (2011).

[11] T. Devaux, V. Tournat, O. Richoux, and V. Pagneux, Asymmetric Acoustic Propagation of Wave Packets via the Self-demodulation Effect, Phys. Rev. Lett. **115**, 234301 (2015).

[12] N. Boechler, J. Yang, G. Theocharis, P. G. Kevrekidis, and C. Daraio, Tunable vibrational band gaps in one-dimensional diatomic granular crystals with three-particle unit cells, J. Appl. Phys. **109**, 074906 (2011).

[13] A. Merkel, V. Tournat, and V. Gusev, Experimental Evidence of Rotational Elastic Waves in Granular Phononic Crystals, Phys. Rev. Lett. **107**, 225502 (2011).

[14] M. Hiraiwa, M. Abi Ghanem, S. P. Wallen, A. Khanolkar, A. A. Maznev, and N. Boechler, Complex Contact-Based Dynamics of Microsphere Monolayers Revealed by Resonant Attenuation of Surface Acoustic Waves, Phys. Rev. Lett. **116**, 198001 (2016).

[15] F. Allein, V. Tournat, V. E. Gusev, and G. Theocharis, Tunable magneto-granular phononic crystals, Appl. Phys. Lett. **108**, 161903 (2016).

[16] L.-Y. Zheng, F. Allein, V. Tournat, V. Gusev, and G. Theocharis, Granular graphene: Direct observation of edge states on zigzag and armchair boundaries, Phys. Rev. B. **99**, 184113 (2019).

[17] M. Molerón, A. Leonard, and C. Daraio, Solitary waves in a chain of repelling magnets, Journal of Applied Physics **115**, 184901 (2014).

[18] B. P. Bernard, B. A. M. Owens, and B. P. Mann, Uncertainty propagation in the band gap structure of a 1D array of magnetically coupled oscillators, J. Vib. Acoust. **135**, 041005 (2013).

[19] F. M. Russell, Y. Zolotaryuk, J. C. Eilbeck, and T. Dauxois, Moving breathers in a chain of magnetic pendulums, Phys. Rev. B **55**, 6304 (1997).

[20] A. Mehrem, N. Jiménez, L. Salmerón-Contreras, X. García-Andrés, L. M. García-Raffi, R. Picó, and V. Sánchez-Morcillo, Nonlinear dispersive waves in repulsive lattices, Phys. Rev. E **96**, 012208 (2017).

[21] J. F. Robillard, O. B. Matar, J. O. Vasseur, P. A. Deymier, M. Stippinger, A. C. Hladky-Hennion, Y. Pennec, and B. Djafari-Rouhani, Tunable magnetoelastic phononic crystals, Appl. Phys. Lett. **95**, 124104 (2009).

[22] J. O. Vasseur, O. B. Matar, J. F. Robillard, A. C. Hladky-Hennion, and P. A. Deymier, Band structures tunability of bulk 2D phononic crystals made of magneto-elastic materials, AIP Adv. **1**, 041904 (2011).

[23] O. Bou Matar, J. F. Robillard, J. O. Vasseur, A. C. Hladky-Hennion, P. A. Deymier, P. Pernod, and V. Preobrazhensky, Band gap tunability of magneto-elastic phononic crystal, J. Appl. Phys. **111**, 054901 (2012).

[24] F. J. Sierra-Valdez, F. Pacheco-Vázquez, O. Carvente, F. Malloggi, J. Cruz-Damas, R. Rechtman, and J. C. Ruiz-Suárez, Acoustic gaps in a chain of magnetic spheres, Phys. Rev. E **81**, 011301 (2010).

[25] A. Palermo, Y. Wang, P. Celli, and C. Daraio, Tuning of Surface-Acoustic-Wave Dispersion via Magnetically Modulated Contact Resonances, Phys. Rev. Applied **11**, 044057 (2019).

[26] V. J. Sanchez-Morcillo, I. Perez-Arjona, V. Romero-Garcia, V. Tournat, and V. E. Gusev, Second-harmonic generation for dispersive elastic waves in a discrete granular chain, Phys. Rev. E **88**, 043203 (2013).

[27] A. Mehrem, N. Jiménez, L. Salmerón-Contreras, X. García-Andrés, L. M. García-Raffi, R. Picó, and V. Sánchez-Morcillo, Nonlinear propagation and control of acoustic waves in phononic superlattices, C. R. Physique **17**, 543 (2016).

[28] R. D. Mindlin, Compliance of elastic bodies in contact, Trans. ASME J. Appl. Mech. **16**, 259 (1949).

[29] L.-Y. Zheng, H. Pichard, V. Tournat, G. Theocharis, and V. Gusev, Zero-frequency and slow elastic modes in phononic monolayer granular membranes, Ultrasonics **69**, 201 (2016).

[30] L.-Y. Zheng, V. Tournat, and V. Gusev, Zero-frequency and extremely slow elastic waves in mechanical granular graphene, Extreme Mech. Lett. **12**, 55 (2017).

[31] H. Pichard, A. Duclos, J.-P. Groby, V. Tournat, and V. E. Gusev, Localized transversal-rotational modes in linear chains of equal masses, Phys. Rev. E 89, 013201 (2014).

[32] C. L. Kane and T. C. Lubensky, Topological boundary modes in isostatic lattices, Nat. Phys. 10, 39 (2014).

[33] T. C. Lubensky, C. L. Kane, X. Mao, A. Souslov, and K. Sun, Phonons and elasticity in critically coordinated lattices, Rep. Prog. Phys. 78, 073901 (2015).

[34] F. Allein, V. Tournat, V. E. Gusev, and G. Theocharis, Transversal–rotational and zero group velocity modes in tunable magneto-granular phononic crystals, Extreme Mech. Lett. 12, 65 (2017).

[35] E. G. Charalampidis, F. Li, C. Chong, J. Yang, and P. G. Kevrekidis, Time-periodic solutions of driven-damped trimer granular crystals, Math. Problems Eng. 2015, 830978 (2015).

[36] C. Chong, F. Li, J. Yang, M. O. Williams, I. G. Kevrekidis, P. G. Kevrekidis, and C. Daraio, Damped-driven granular chains: An ideal playground for dark breathers and multibreathers, Phys. Rev. E 89, 032924 (2014).

[37] C. Hoogeboom, Y. Man, N. Boechler, G. Theocharis, P. G. Kevrekidis, I. G. Kevrekidis, and C. Daraio, Hysteresis loops and multi-stability: From periodic orbits to chaotic dynamics (and back) in diatomic granular crystals, Europhys. Lett. 101, 44003 (2013).

[38] E. B. Herbold and V. F. Nesterenko, Shock wave structure in a strongly nonlinear lattice with viscous dissipation, Phys. Rev. E 75, 021304 (2007).

[39] R. Carretero-González, D. Khatri, Mason A. Porter, P. G. Kevrekidis, and C. Daraio, Dissipative Solitary Waves in Granular Crystals, Phys. Rev. Lett. 102, 024102 (2009).

[40] A. Merkel, G. Theocharis, F. Allein, J.-P. Groby, V. Gusev, and V. Tournat, Testing a bead-rod contact with a nonlinear resonance method, J. Sound Vib. 441, 84 (2018).

[41] G. Kuwabara and K. Kono, Restitution coefficient in a collision between two spheres, Jap. J. Appl. Phys. 26(Part 1, No. 8), 1230 (1987).

[42] N. V. Brilliantov, F. Spahn, J.-M. Hertzsch, and T. Poschel, Model for collisions in granular gases, Phys. Rev. E 53, 5382 (1996).

[43] N. V. Brilliantov, A. V. Pimenova, and D. S. Goldobin, A dissipative force between colliding viscoelastic bodies: Rigorous approach, Europhys. Lett. 109, 14005 (2015).

[44] R. P. Moiseyenko and V. Laude, Material loss influence on the complex band structure and group velocity in phononic crystals, Phys. Rev. B 83, 064301 (2011).

[45] G. Theocharis, O. Richoux, V. Romero-Garcia, A. Merkel, and V. Tournat, Limits of slow sound propagation and transparency in lossy, locally resonant periodic structures, New J. Phys. 16, 093017 (2014).

[46] J. Cabaret, V. Tournat, and P. Béquin, Amplitude-dependent phononic processes in a diatomic granular chain in the weakly nonlinear regime, Phys. Rev. E 86, 041305 (2012).